American Mineralogist, Volume 91, pages 1739–1746, 2006

Effects of natural radiation damage on back-scattered electron images of single crystals of minerals

LUTZ NASDALA,[1,*] ANDREAS KRONZ,[2] JOHN M. HANCHAR,[3] MARION TICHOMIROWA,[4] DONALD W. DAVIS,[5] AND WOLFGANG HOFMEISTER[1]

[1]Institut für Geowissenschaften—Mineralogie, Johannes Gutenberg-Universität, D-55099 Mainz, Germany
[2]Geowissenschaftliches Zentrum der Georg-August-Universität Göttingen, D-37077 Göttingen, Germany
[3]Department of Earth Sciences, Memorial University of Newfoundland, St. John's, Newfoundland A1B 3X5, Canada
[4]Institut für Mineralogie, Technische Universität Bergakademie Freiberg, D-09596 Freiberg, Germany
[5]Department of Geology, University of Toronto, Toronto, Ontario M5S 3B1, Canada

ABSTRACT

Generally, it has been assumed that signal intensity variations in back-scattered electron (BSE) images of minerals are mainly controlled by chemical heterogeneity. This is especially true for images of single crystals, where effects of different crystal orientations with respect to the incident beam on the observed BSE are excluded. In contrast, we show that local variations of the structural state within single-crystals (i.e., degree of lattice order or lattice imperfectness) may also have dramatic effects on the back-scattering of electrons. As an example, we present BSE images of single-crystals of natural zircon, $ZrSiO_4$, whose intensity patterns are predominantly controlled by structural heterogeneity, whereas effects of chemical variations are mostly negligible. In the case of natural zircon, structural heterogeneity affecting the BSE patterns is predominantly due to heterogeneous accumulation of radiation damage. We attempt to explain our observations with lowered penetration and channeling and, thus, enhanced back-scattering of electrons in more radiation-damaged internal zones and micro-areas. Back-scattered electron contrast of natural zircon is, therefore, considered as a special case of electron channeling contrast. This phenomenon seems to have been generally underappreciated in the discussion of BSE images of radiation-damaged minerals thus far.

Keywords: Electron microscopy, BSE imaging, Raman spectroscopy, zircon

INTRODUCTION

Zircon ($ZrSiO_4$) is an orthosilicate mineral that generally incorporates trace amounts of actinide elements (i.e., U and Th), and other trace and minor elements including Hf, P, Y, and the rare earth elements (REEs). The decay of U and Th to form radiogenic Pb over geologic time generates structural damage in zircon, up to the complete loss of crystallinity in the so-called "metamict" state (e.g., Chakoumakos et al. 1987; Ewing 1994). On the other hand, the zircon U-Th-Pb isotopic system is one of the most widely used and robust geochronometers. Zircon occurs in many types of igneous, metamorphic, and sedimentary rocks. It is characterized by remarkable durability and stability against melting, dissolution, and secondary alteration, leading to an extraordinary geologic memory. The latter is often reflected by complicated internal textures (Lork and Koschek 1991; Paterson et al. 1992; Hanchar and Miller 1993; Hanchar and Rudnick 1995; Vavra et al. 1996; Corfu et al. 2003), which may include primary growth zoning, sectoral zoning, inherited cores, metamorphic overgrowth rims, or recrystallization patches. It has, therefore, become routine to use back-scattered electron (BSE) images, often in combination with cathodoluminescence (CL) images, to reveal internal features and to thereby constrain age determinations from in situ zircon U-Th-Pb isotopic data.

Internal contrast patterns observed using BSE are visible due to local variations of the fraction of primary electrons that escape after back-scattering (i.e., deflection through an angle of >90°); the latter is described by the back-scatter coefficient η. This coefficient increases with increasing average atomic number ($\overline{Z}$; Hall and Lloyd 1981; Lloyd 1987), which is due to the higher number of charge carriers of higher Z elements (Donovan et al. 2003). Note that BSE should not be described as luminescence (e.g., Wang and Griffin 2004); luminescence phenomena are related to the secondary emission of photons upon energetic transitions of electrons in the sample whereas, in contrast, the BSE signal is due to elastic scattering of incident-beam electrons.

According to our cautious estimates, hundreds of thousands of BSE images of zircon have been taken in the past two decades; and hundreds of them have been published in international peer-reviewed journals. Until now, it has been generally assumed that internal variations of the BSE intensity within zircon single crystals are due to $\overline{Z}$ variations as caused by chemical heterogeneity. Such $\overline{Z}$ variations are mostly assigned to enhanced concentrations of higher Z elements such as Hf and U and, to a lesser extent, Th, Y, and Yb (e.g., Sommerauer 1976; Hanchar and Miller 1993; Benisek and Finger 1993; Hanchar and Rudnick 1995; Hartmann et al. 1997; Guan et al. 2002; Crowley 2003), but have also been interpreted to be caused by the incorporation of lower Z species such as water, Ca, and P (Booth et al. 2005). Other

* Present address: Institut für Mineralogie und Kristallographie, Universität Wien, A-1090 Wien, Austria. E-mail: lutz.nasdala@univie.ac.at

factors, such as surface topography effects or crystal orientation contrast (Christenhuss 1968; Joy et al. 1982; Lloyd 1987; Trimby and Prior 1999; Day and Quested 1999; Prior et al. 1999), are generally assessed as insignificant for the BSE signal of natural zircon, especially if variations within single crystals in mounts with a flat polished sample surface are discussed.

In contrast to all previous assumptions, we report in the present paper that the structural state of zircon (i.e., its degree of structural radiation damage) is the primary controlling factor of the BSE intensity; radiation-damaged zircon yields in most cases significantly enhanced BSE intensity, with a strong dependence on the degree of metamictization.

Samples and experimental details

We have studied natural zircon single-crystals (lengths ranging from 150 to 350 µm) from six rocks, whose ages scatter between Archean and Neogene. The majority of crystals studied here are heterogeneous, i.e., internally zoned. Zircon samples were obtained from the following lithologies and localities. (1) A gabbro from the Mulcahy Lake intrusion, Ontario (age 2733 ± 1 Ma; Morrison et al. 1985). (2) The Bluffpoint quartz diorite, Atikwa–Lawrence Batholith, Ontario [age 2732 ± 1 Ma (D.W. Davis, unpublished); for rock description cf. Davis and Edwards 1985]. (3) A monzogranitic gneiss from Afella, In Ouzzal massif, Algeria (age 1983 ± 15 Ma; Peucat et al. 1996). (4) A potassium-rich leucogranite located near Dannemora, Adirondack Mountains, New York [age ~1045–1050 Ma (J.M. Hanchar and M.J. Whitehouse, unpublished); for rock description cf. McLelland et al. 2001]. (5) A granodiorite from Demitz, Lusatia, Germany (age 533 ± 5 Ma; Tichomirowa et al. 2001). And (6) a rhyolite tuff from the Gyulakeszi formation, located near Pécs, Hungary (age 19.6 ± 1.4 Ma; Harangi 2001). We also studied a synthetic, pure $ZrSiO_4$ crystal grown using the Li-Mo flux technique (Hanchar et al. 2001).

The preparation of zircon crystals is elucidated in Figure 1. Zircon single-crystals were cut in two halves, parallel to their *c* axis. Cutting was done with a 5 µm thick tungsten wire and glycerine-diamond suspension, using a microtome system described by Sergeev et al. (1997). One half of each crystal was then subjected to heat-treatment in air to anneal the radiation damage, whereas the other half remained in its natural, radiation-damaged state. Half-crystals to be heated were placed on a platinum foil and heated up to 1300 °C, at a rate of 10°/min. At the end of the 96 hour treatment at 1300 °C, the furnace was switched off. The furnace door was not opened for additional 24 hours, after which time the samples had cooled to room temperature. Both the annealed and naturally radiation-damaged half-crystals of each sample were then embedded in epoxy and prepared in close proximity to each other in one polished mount. All pairs of crystal halves (with the exception of sample 80A; Figs. 2I–J) were prepared with their crystallographic *c* axes parallel to each other, to minimize potential effects of different crystal orientations. For electron probe microanalyzer (EPMA) and scanning electron microscope (SEM) analysis, mounts were coated with carbon.

The degree of radiation damage of zircon micro-areas was estimated from the increasing FWHM (full width at half band-maximum) of the antisymmetric $\nu_3(SiO_4)$ stretching vibration (B_{1g} vibrational mode at ~1000 cm^{-1}) determined in situ by confocal Raman spectroscopy (Nasdala et al. 1995). Raman measurements were done with a Horiba Jobin Yvon LabRAM HR 800 using He-Ne 632.8 nm excitation. Experimental details are reported elsewhere (Nasdala et al. 2005). The correction of measured FWHMs for the system's spectral resolution (in detail discussed by Nasdala et al. 2001b) was done according to the method of Irmer (1985). Raman maps (see Lehnert 2000) consisting of 50 000–80 000 single spectra were obtained using a software-controlled *x*-*y* stage. Color-coded images (i.e., distribution patterns for a certain spectroscopic parameter) were then produced after appropriate data reduction. It has been shown that the impact of the focused electron beam during EPMA analysis of radiation-damaged zircon may cause partial structural reconstitution (Nasdala et al. 2002, 2003). To avoid such analytical artifacts, Raman point measurements and mappings were always done before the EPMA analyses.

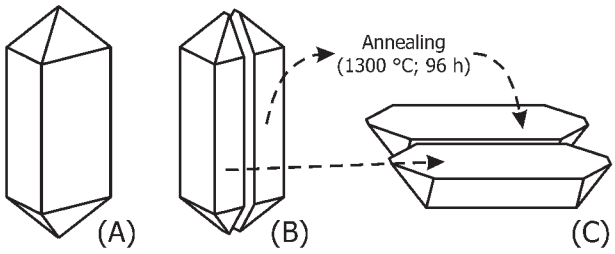

Figure 1. Sketch of the sample preparation process. Zircon crystals (**A**) were cut parallel to their *c* axis (**B**). Only one half of each crystal was heat-treated whereas the other half remained in its natural, radiation-damaged state. Both half-crystals were then embedded in epoxy and prepared close to each other in one mount (**C**), to make it possible to obtain the BSE (or CL) signal of both of them together in one single image.

Imaging (BSE and CL) was done using a JEOL 8900 RL EPMA at 20 nA beam current and an accelerating voltage of 20 kV, and a LEO Gemini 1530 SEM using 1.5 nA beam current and 10 kV accelerating voltage. Chemical compositions of samples were determined using the EPMA, operated at 20 kV and a beam current of 30 nA. Details on the EPMA analyses are reported elsewhere (Nasdala et al. 2005). Mean atomic numbers ($\overline{Z}$) were calculated according to (Pouchou and Pichoir 1991)

$$\overline{Z} = \left(\sum_i C_i \sqrt{Z_i}\right)^2 \quad (1)$$

with C_i = weight (mass) concentration and Z_i = atomic number of element *i*.

Results

General chemical compositions of micro-areas in zircon crystals, calculated $\overline{Z}$ values, $\nu_3(SiO_4)$ Raman band FWHMs, and BSE intensities are presented in Table 1, and images and Raman maps are shown in Figure 2. Zircon samples (i.e., un-annealed crystal halves) cover a range from slightly radiation-damaged to strongly metamict. High levels of radiation damage are indicated by FWHM values larger than 20 cm^{-1}, as observed in micro-areas with the highest BSE intensities in samples A1 (Figs. 2A–D) and 80A (Figs. 2I–J). Low FWHMs ≤5 cm^{-1} characterize a zircon micro-area as well crystalline to slightly radiation-damaged; examples include the Neogene sample M2 (Fig. 2K), the low-BSE overgrowth region of sample 31E (Fig. 2E–H), and, of course, all annealed crystal halves. Note, however, that annealing at 1300 °C for four days has annealed the majority of radiation damage, but was still insufficient to reach always complete structural reconstitution (cf. scatter of Raman FWHMs of annealed halves in Table 1); this corresponds to previous observations reported by Nasdala et al. (2002).

In contrast to previous assumptions, we did not find a clear correlation between BSE intensity and $\overline{Z}$ (Fig. 3A). Observed BSE intensities, however, show a remarkably strong correlation with the degree of radiation damage, with more radiation-damaged micro-areas yielding more intense BSE (Fig. 3B). The purpose of doing annealing experiments in this study was to demonstrate the latter observation more clearly. High-temperature treatment under dry conditions causes structural reconstitution of initially radiation-damaged zircon but only minor changes in its chemical composition. Comparative analyses of recrystallized annealing products and their radiation-damaged starting materials in the matching face therefore allowed us to investigate effects of the structural state on the BSE intensity without having to consider significant differences in chemical composition and, with that, $\overline{Z}$ values. For this, flat polished epoxy mounts were prepared with the un-annealed and annealed half of each crystal placed next to each other. This procedure (see again Fig. 1) made it possible to obtain one BSE image showing both halves of each crystal (Figs. 2B, F, I, K, and L), allowing truly uniform experimental

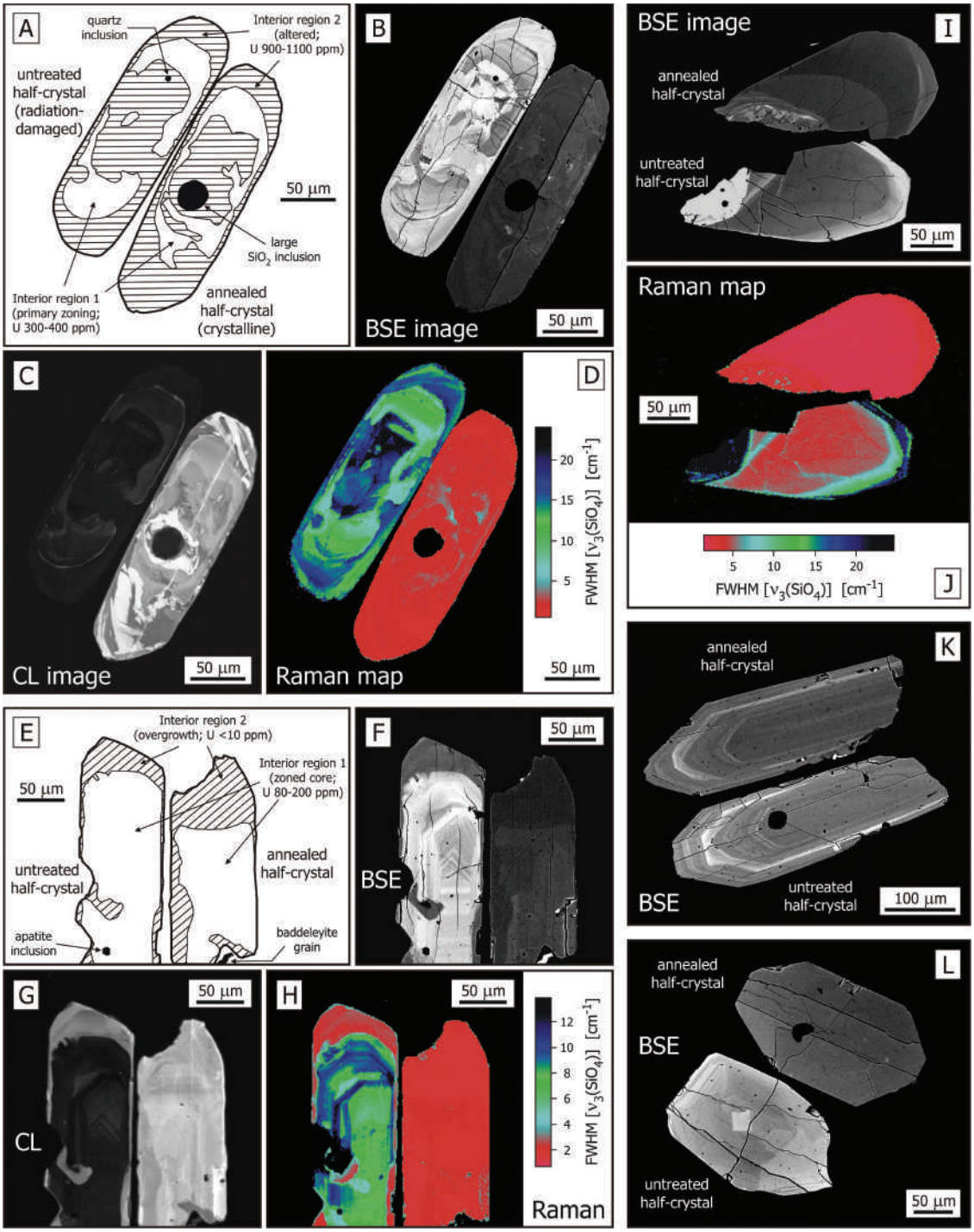

FIGURE 2. Images of cut zircon crystals, always showing the heat-treated crystal half in close proximity to its naturally radiation-damaged analog. (**A–D**) Simplified sketch of the internal texture, BSE image, CL image, and color-coded Raman map of a zircon crystal from a leucogranite, Adirondack Mountains, New York (sample A1). (**E–H**) Same sequence of images of a zircon crystal from the Mulcahy Lake gabbro, Ontario (sample 31E). (**I–J**) BSE image and Raman map of a gneiss zircon from Afella, Algeria (sample 80A). In the three Raman maps (**D**, **H**, and **J**), each pixel in images represents an analysis of the Raman band FWHM. In all three cases (**B** and **D**; **F** and **H**; **I** and **J**) the BSE intensity distribution correlates very well with the degree of structural disorder as revealed by the increasing Raman band FWHM. (**K**) BSE image of a rhyolitic tuff zircon, Hungary (sample M2). (**L**) BSE image of a zircon from the Bluffpoint quartz diorite, Ontario (sample 81-32). Intensities of the BSE (and CL) images cannot be directly compared, because intensity gain and contrast were individually adjusted to make internal textures recognizable. Note, however, that all BSE and CL subfigures (**B**, **C**, **F**, **G**, **I**, **K**, and **L**) are direct images and not graphically mounted; i.e., the two crystal halves (i.e., un-annealed and annealed halves) were always imaged together in one step.

TABLE 1. Electron probe microanalysis results, Raman data, and BSE intensities for samples investigated

Zone*	EPMA data (wt% oxide) and calculated $\bar{Z}$													
	ZrO_2	SiO_2	HfO_2	P_2O_5	Y_2O_3	Dy_2O_3	Er_2O_3	Yb_2O_3	ThO_2	UO_2	Total	$\bar{Z}$	FWHM† (cm^{-1})	BSE‡ (a.u.)
Sample 31E (Mulkahy Lake gabbro)														
N-1a	66.6	32.2	0.75	0.04	0.14	<0.04	<0.04	<0.05	<0.02	0.03	99.7	22.30	10.0	144
N-1b	67.1	32.3	0.79	0.05	0.14	<0.04	<0.04	0.05	<0.02	0.02	100.5	22.74	9.6	130.5
N-2	67.6	32.3	0.54	<0.03	<0.03	<0.04	0.04	0.05	<0.02	<0.02	100.6	22.69	2.1	55.5
A-1a	67.0	32.4	0.82	0.06	0.17	<0.04	0.05	<0.05	<0.02	0.02	100.4	22.70	2.0	48.9
A-1b	66.6	32.4	0.88	<0.03	0.19	<0.04	0.04	<0.05	<0.02	0.02	100.1	22.53	1.9	55
A-2	66.9	32.6	0.63	<0.03	<0.03	<0.04	<0.04	<0.05	<0.02	<0.02	100.2	22.47	1.9	41.8
Sample 81-32 (Bluffpoint quartz diorite)														
N-1a	66.8	32.4	1.02	0.04	0.07	<0.04	0.04	<0.05	<0.02	0.03	100.5	22.73	8.1	132.6
N-1b	66.6	32.8	1.03	0.05	0.08	0.04	0.04	<0.05	<0.02	<0.02	100.6	22.73	8.1	139.3
N-2a	67.4	32.4	0.81	0.04	0.10	<0.04	<0.04	<0.05	<0.02	0.03	100.8	22.87	5.3	111.2
N-2b	67.6	32.3	0.97	0.04	0.10	<0.04	<0.04	0.05	<0.02	0.02	101.0	23.04	4.8	92.5
N-3	67.0	32.2	0.84	0.05	0.17	<0.04	0.07	<0.05	<0.02	<0.02	100.3	22.64	7.7	132.5
A-1	67.1	32.6	1.11	0.03	0.06	<0.04	<0.04	<0.05	0.02	<0.02	100.9	22.66	2.0	68
A-2	67.0	32.6	0.84	0.06	0.17	<0.04	0.10	<0.05	<0.02	<0.02	100.7	22.71	1.9	74.3
Sample 80A (Afella gneiss)														
N-1	64.8	33.0	1.78	0.07	0.52	<0.04	0.09	0.17	0.06	0.14	100.6	22.93	24.4	212.8
N-2a	67.3	32.0	1.65	0.06	0.06	<0.04	0.05	<0.05	<0.02	0.08	101.2	23.36	19.9	196.7
N-2b	66.9	32.5	1.62	0.05	0.07	0.04	0.05	<0.05	<0.02	0.09	101.3	23.29	16.5	197.5
N-3a	66.6	32.6	1.20	0.09	0.09	<0.04	0.07	<0.05	<0.02	<0.02	100.7	22.86	5.2	97.9
N-3b	66.8	32.6	1.06	0.08	0.08	<0.04	0.05	<0.05	<0.02	0.02	100.7	22.84	5.6	95.6
A-1	65.3	32.5	1.77	0.13	0.42	<0.04	0.12	0.11	0.04	0.14	100.6	22.98	3.5	101
A-2	66.6	32.0	1.59	0.05	0.07	<0.04	0.07	<0.05	<0.02	0.08	100.4	22.92	2.8	93
A-3	66.9	32.1	1.07	0.09	0.07	<0.04	0.05	0.05	<0.02	<0.02	100.4	22.78	2.3	72.9
Sample A1 (Adirondacks leucogranite)														
N-1	66.6	32.0	1.31	0.04	0.10	<0.04	0.04	<0.05	<0.02	0.04	100.1	22.71	7.6	136
N-2a	66.8	32.1	1.27	<0.03	0.04	<0.04	<0.04	<0.05	<0.02	0.12	100.3	22.83	16.9	196.6
N-2b	66.1	31.8	1.27	<0.03	0.05	<0.04	<0.04	<0.05	<0.02	0.12	99.4	22.40	17.1	200.8
N-3	65.0	31.7	0.98	0.13	0.79	0.04	0.15	0.16	0.08	0.19	99.2	22.35	25.4	216.7
A-1	66.7	32.2	1.26	0.05	0.13	<0.04	0.04	<0.05	<0.02	0.05	100.4	22.79	2.1	78.9
A-2	65.6	32.5	1.26	<0.03	0.03	<0.04	<0.04	<0.05	<0.02	0.10	99.5	22.32	1.8	80.7
Sample D1 (Demitz granite)														
N-a	65.5	32.6	0.75	0.16	0.66	0.07	0.12	0.13	0.02	0.03	100.1	22.47	5.7	97.6
N-b	65.7	32.5	0.72	0.13	0.69	<0.04	0.13	0.14	0.02	0.03	100.0	22.52	5.5	95.9
A-a	65.8	32.7	0.76	0.11	0.81	0.10	0.15	0.16	0.03	0.03	100.6	23.18	2.7	94
A-b	66.0	32.6	0.72	0.15	0.68	0.06	0.12	0.09	0.06	0.03	100.6	22.78	2.7	86.1
Sample M2 (Hungary rhyolite tuff)														
N	66.7	32.8	0.96	0.03	0.11	<0.04	0.05	<0.05	<0.02	0.03	100.7	22.78	2.7	93.2
A-a	66.7	32.6	0.89	0.05	0.19	<0.04	<0.04	<0.05	<0.02	0.03	100.5	22.70	2.5	75.9
A-b	66.8	32.7	0.84	0.08	0.28	<0.04	0.10	0.10	0.04	0.04	100.9	22.91	2.5	77.3
Synthetic $ZrSiO_4$														
	67.6	32.8	<0.07	<0.03	<0.03	<0.04	<0.04	<0.05	<0.02	<0.02	100.4	22.41	1.8	21

Notes: Alumina, Ca, Fe, and Ho have also been analyzed. Data are not reported here because these elements were in most cases below the detection limit of our EPMA.

* N = naturally damaged, un-annealed, zircon sample; A = annealed zircon sample. Number after letter A or N (if applicable) refers to internal zones of the zircon grain. Letter after number refers to analysis number within a given zone.

† FWHM = real (i.e., corrected) full width at half band maximum of the $\nu_3(SiO_4)$ Raman band.

‡ BSE = intensities on an arbitrary grayscale, based on uniform imaging conditions for all samples.

conditions and thus direct comparison of BSE intensities. Note that within pairs of crystal halves, internal textures show the same zircon zones, but somewhat different patterns (see for instance Fig. 2E: corresponding interior regions have different relative extension), and inclusions of other minerals are often seen in only one half-crystal (Fig. 2A). This is explained by the loss of material in the preparation process (cutting, grinding, polishing); we estimate that polished faces of crystal halves correspond to two parallel planes that were about 15–20 μm apart from each other in the original crystal.

Annealing of radiation damage resulted in a dramatic increase of the cathodoluminescence (CL) emission (Nasdala et al. 2002; Figs. 2C, G of present paper) and a decrease in the BSE intensity. The η decrease upon annealing is particularly strong where the starting material was affected by strong radiation damage (e.g., sample A1 in Fig. 2B; outer rim and core of zircon 80A, Fig. 2I). In contrast, annealing zircon with low levels of radiation damage had only minor effects on η (e.g., low-actinide rim of sample 31E, Fig. 2F; Neogene tuff zircon M2, Fig. 2K; sample D1).

All zircon samples investigated in the present study showed the "normal" behavior of (1) inversely correlated BSE and CL and (2) higher electron back-scattering from more metamict micro-areas. There exist, however, rare exceptions: It has long been known that zircon affected by secondary processes may yield particularly low BSE (Peterman et al. 1986; Pointer et al. 1988; Smith et al. 1991; Irber et al. 1997; Kempe et al. 2000). Such samples, or micro-areas within samples, are typically characterized by anomalously low totals of EPMA analyses (often close to or even below 90% on a wt% oxide basis). Low totals, and related very low BSE intensities, were ascribed to high content of hydrous species (Peterman et al. 1986; Smith et al. 1991), vacancies (Kempe et al. 2000), or sub-micrometer sized voids (Pointer et al. 1988); however, detailed studies still need to be done before this can be resolved.

Before discussing the generally increased BSE intensity of radiation-damaged zircon as observed in this study, we felt we were obliged to critically check for potential artifacts that may affect our interpretations. The possibility that the observed η

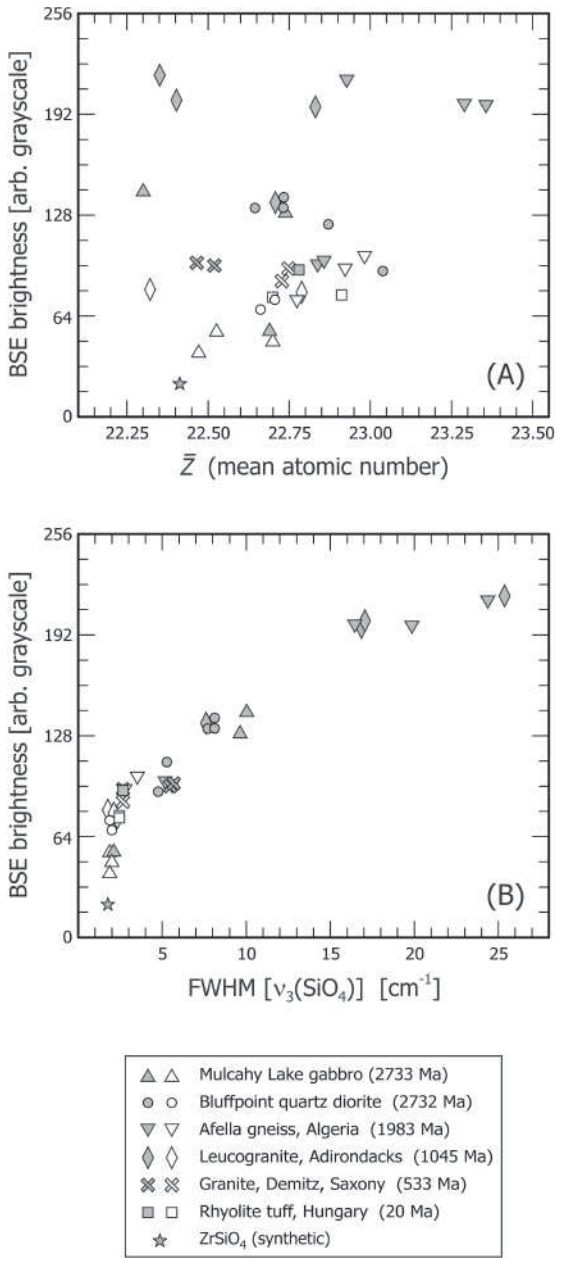

FIGURE 3. Plots of the BSE intensity vs. mean atomic number (**A**) and Raman band broadening, indicating the degree of radiation damage (**B**). Data pairs for natural zircon samples from six localities and synthetic pure $ZrSiO_4$ are shown. Gray symbols, untreated half-crystals; open symbols, annealed half-crystals. Note that plotted BSE intensities (see Table 1) do *not* correspond to the BSE images shown in Figure 2. Plotted values were obtained under uniform conditions for all samples (i.e., using the same sample and instrument conditions and grayscale settings on the BSE detector).

decrease upon annealing is connected with an unrecognized $\bar{Z}$ decrease due to the loss of non-analyzed elements can be excluded. Annealed zircon crystals are expected to differ from their starting material due to the loss of radiogenic lead and helium (produced through alpha-decay events), and hydrous species. Lead loss (which, due to the slow volume diffusion of Pb, is likely a consequence of the recrystallization process that may involve grain boundary diffusion, rather than volume diffusion; Cherniak and Watson 2001) would decrease $\bar{Z}$. This, however, is assessed as insignificant for our case because of generally low Pb concentrations in natural zircon. For instance, even if a sample contained 0.1 wt% (i.e., 1000 ppm) of Pb (N.B. which is unusually high for natural zircon), complete Pb loss would change $\bar{Z}$ by only –0.04, which is clearly insufficient to explain the observed η decrease (compare Table 1 and Fig. 3A). Helium (Reiners et al. 2004) and hydrous species (Caruba et al. 1985; Nasdala et al. 2001a) are likely to have escaped completely during the heat-treatment. Resulting effects (e.g., $\bar{Z}$ increase), however, must also be insignificant because they should result in an increase in η.

It is also well known that η varies with the crystal orientation (Christenhuss 1968; Joy et al. 1982; Lloyd 1987): Depending on the angle of the incident beam relative to the lattice, varying fractions of primary electrons may channel deeper into the sample, which in turn reduces their back-scattered fraction. This is used in crystal orientation contrast images; recently, an example for zircon has been published by Reddy et al. (2006). Such effects, however, can also be excluded as the main cause for the BSE intensity variations observed from our samples. First of all, η variations within zoned single crystals are discussed. Second of all, preliminary oriented Raman and single-crystal X-ray analyses revealed that the crystallographic orientation of annealing products corresponds to their natural analogs (i.e., crystallographic *c* axis parallel to prism faces). Because pairs of crystal halves were prepared with their *c* axes parallel to each other, there are no notable differences in the crystallographic orientation of the two neighbored crystal halves (exception: sample 80A in Figs. 2I–J). Third, principal BSE patterns (i.e., more metamict micro-areas always yield brighter BSE; see Figs. 2B, F, I, K, and L) are observed independent from the angle between incident beam and crystal lattice. This was checked by tilting samples in an SEM and comparing the BSE images. Even though observed absolute intensities differed to some extent, depending on the tilt angle (which is, see above, explained by different channeling conditions under different crystal orientations), we always found the natural radiation damaged halves to appear brighter than annealed halves. In contrast, if observed BSE intensities were controlled by variations of the crystal orientation, tilting samples should have resulted in dramatic changes, and even reversal, of BSE brightness ratios (demonstrated by Christenhuss 1968).

The possibility that BSE detectors are affected by signals other than back-scattered electrons can also be excluded. It is well known that some BSE detectors are sensitive to light photons, which is why strong CL may, as an analytical artifact, in some cases enhance the apparent BSE intensity. If this was the case, however, the observed CL and (apparent) BSE patterns should correlate. In contrast, we found high BSE intensities in micro-areas with low CL emission and vice versa (e.g., Figs. 2B–C and 2F–G). That phenomenon has been reported previously (Hanchar and Miller 1993; Nasdala et al. 2002; Corfu et al. 2003). Finally, enhanced quantities of secondary electrons (SE) can also be excluded; the samples investigated appeared fairly homogeneous in SE imaging mode and charging effects were not observed.

Discussion and conclusions

Our results suggest that the elemental composition (e.g., primarily variations in Hf and U) has only a minor effect on the BSE signal; whereas internal η variations in natural zircon crystals are primarily controlled by the structural state of this mineral. This effect seems to have been overlooked in the past (Paterson et al. 1992; Hanchar and Miller 1993; Hanchar and Rudnick 1995; Corfu et al. 2003), perhaps due to the fact that absolute BSE intensities are normally not of analytical interest in imaging internal textures of natural zircon crystals. Instead, signal gain and contrast of the BSE image are usually readjusted individually from image to image to make internal features of zircon crystals recognizable as clearly as possible for other purposes such as in situ U-Th-Pb isotopic, trace element, or other studies. Also, we may speculate that the correlation between η and radiation damage has been overlooked, and η has been misinterpreted to depend mainly on $\overline{Z}$, because radiation-damaged zircon is often characterized by enhanced concentrations of higher *Z* elements such as hafnium or uranium.

With our conclusion, however, we do not attempt to generally deny $\overline{Z}$ effects on the BSE of zircon. For instance, annealing the radiation damage has caused only a minor decrease of the BSE intensity of the Neogene tuff zircon sample M2 (Fig. 2K). This is explained by the consideration that, due to its low actinide content and young age and the correspondingly low self-irradiation dose, this zircon is only slightly radiation-damaged (cf. Raman data in Table 1). The weak BSE zoning of both the natural and the annealed crystal half of this sample (only observed after significant amplification of the BSE contrast) are assigned to modest $\overline{Z}$ variations among growth zones. A much clearer example for the $\overline{Z}$ dependence of zircon BSE images was recently published by Geisler et al. (2005) who described zircon crystals from the so-called "Chernobyl lava." These zircon crystals (their age was less than 20 years; they were produced in the nuclear accident in April 1986) were found to contain up to ~15 wt% UO_2, and their BSE images correlate closely with element distribution patterns. Also, Hanchar et al. (2001) showed that the BSE of synthetic zircon crystals doped with individual rare earth elements and Y, and phosphorus, correlates very well with the strong $\overline{Z}$ variations in these crystals. Natural zircon crystals, however, rarely incorporate large amounts of non-formula elements, aside from Hf, and thus normally show only minor internal $\overline{Z}$ variations, which, in turn, have comparably small effects on the BSE.

In the following, we attempt to interpret our observation that in the case of radiation-damaged zircon, BSE intensities correlate with the degree of structural damage; however, a fully unequivocal hypothesis cannot be presented at the present stage. Because chemical variations are excluded as the major factor controlling the BSE in natural single crystals, we need to consider effects of the structural state of zircon on the electron back-scattering. Besides the above discussed crystal orientation contrast, there are other examples for effects of the crystal structure on the BSE. Materials with the same chemical composition (and, with that, the same $\overline{Z}$) but different structures may yield different BSE intensities. This is commonly referred to as BSE phase contrast (in geologic samples normally overlaid by crystal orientation contrast). An example for geologic materials was reported by Mosenfelder (2000) who observed different BSE intensities of coesite compared to stishovite. Also, it is well known that structural damage of solids affects η, which is—similar to crystal orientation effects—related to changes in the electron channeling behavior of the material. Electron channeling contrast imaging (ECCI) is therefore applied to image structural imperfectness and heterogeneity, including enhanced concentrations of defects, dislocations, and strain, in radiation-damaged (Mitchell and Day 1998) and other materials (Maurice et al. 1969; Zauter et al. 1992; Schwab et al. 1996; Simkin and Crimp 2000; Wu et al. 2002; Kaneko et al. 2005).

In the case of natural zircon single-crystals, local η variations must be due to the particular nanometer-scale structure of radiation-damaged zircon, which consists of a three-dimensional network of disordered crystalline remnants and amorphous clusters (Murakami et al. 1991; Weber et al. 1994; Salje et al. 1999). It appears likely that the higher density of structural defects in radiation-damaged zircon (including point defects and crystalline-amorphous boundaries) decreases the average penetration depth of incident-beam electrons and the probability of electron channeling and, with that, increases η. Therefore, we consider BSE images of radiation-damaged zircon crystals to represent a special case of electron channeling contrast. An alternative hypothesis relates the higher BSE intensity to ionization and charge imbalance, for instance "electron trapping" at defect centers, in radiation-damaged zircon. Such effects would then be comparable to charge contrast images of defect structures in minerals as obtained in the environmental SEM (Baroni et al. 2000). However, if charging affected our zircon BSE images, it should have been observed in SE images also; this was not the case.

To avoid confusion in the interpretation of ECCI images, note that with increasing lattice imperfectness, micro-areas appear darker in transmission electron microscope (TEM) images (which is due to the lower fraction of transmitted electrons) but brighter in SEM images (higher fraction of back-scattered electrons). For better comparability of TEM and SEM images, it has become commonplace (especially in the materials science literature) to invert SEM images. The reader should, therefore, always check carefully whether BSE images taken in an SEM have, or have not, been inverted. In our study, BSE images have not been inverted but are shown as obtained. Also note that (in our case comparably strong) electron channeling effects are observed under virtually random sample orientation with respect to the incident beam (though, as reported above, with moderate absolute intensity variations); they should therefore not be confused with diffraction-dependent channeling effects such as the so-called Kikuchi patterns that are observed using the electron back-scatter diffraction (EBSD) technique.

For future studies of the relationships between the structure and BSE variations in natural zircon, it appears worthwhile to use BSE imaging in combination with Raman spectroscopy, TEM, and EBSD; recently, the latter has been applied to characterize the radiation damage of zircon micro-areas (N.J. Cayzer, personal communication). Studies are also planned to quantify as to which portion the electron back-scattering of other minerals and solids is affected by chemical and/or structural factors. For instance, η variations in monazite (this mineral is commonly character-

ized by much more extensive chemical variations than zircon; Förster 1998) are generally assumed to depend on $\overline{Z}$ (e.g., Zhu et al. 1997). Our present observations, however, imply that effects of heterogeneous radiation damage on η variations within monazite single crystals cannot be excluded from the outset. Annealing experiments followed by comparative SEM imaging of actinide-bearing orthophosphate minerals are planned to address this question.

The correlation between BSE intensity and the degree of radiation damage in natural zircon opens up new possibilities to use the "conventional" BSE imaging as a simple means for studying processes of radiation damage accumulation. This is especially true for the study of virtually non-luminescent phases, i.e., where CL imaging cannot be used. Back-scattered electron imaging may thus prove particularly useful in the investigation of synthetic minerals and self-irradiation of ceramic waste forms containing short-lived alpha emitters such as ^{238}Pu or ^{241}Am. It may also be worthwhile to reconsider previous interpretations of zircon BSE images. To give an example, the observation of strong BSE intensity variations within zircon crystals has, up to now, generally been interpreted to indicate strong chemical heterogeneity. According to our results, in contrast, the same observation indicates intense and heterogeneously distributed radiation damage (which, for instance, enables one to exclude a young annealing event in the sample's geologic history).

We have observed that upon thermal annealing of the radiation damage, the majority of BSE variations within zircon single crystals is virtually lost in most cases (see again Figs. 2B, 2F, 2I, and 2L). Consequently, BSE images of radiation-damaged zircon crystals are in most cases virtual maps of radiation damage distribution (with the exception of the above discussed "unusually low" BSE of certain altered/overprinted zircon). The obvious conclusion that causes of BSE variations seem to have been misinterpreted in the past does not affect the benefit of BSE images and their excellent ability to reveal internal growth and alteration textures of minerals and other ceramic materials. Interpretative terms such as "atomic-number contrast images" or "$\overline{Z}$-contrast images" (e.g., Utsunomiya et al. 2004), however, should not be used anymore in the description and discussion of BSE images of natural zircon.

ACKNOWLEDGMENTS

We are indebted to I. Oláh and J.J. Peucat for providing zircon samples and D. Dettmar for preparation of the high quality epoxy mounts. Thanks are due to N. Groschopf, T. Häger, and E. Wessel for experimental help, and to S.A. Bowring, J.J. Donovan, M. Fueting, C. Holste, R. Mason, P.W. Reiners, W. Tirschler, and A. Zaitsev and for stimulating discussions. Constructive reviews of F. Corfu and B.J. Griffin helped to improve the manuscript. Funding for this research was provided by the Materials Science Research Centre, Mainz.

REFERENCES CITED

Baroni, T.C., Griffin, B.J., Browne, J.R., and Lincoln, F.J. (2000) Correlation between charge contrast imaging and the distribution of some trace level impurities in gibbsite. Microscopy and Microanalysis, 6, 49–58.

Benisek, A. and Finger, F. (1993) Factors controlling the development of prism faces in granite zircons: a microprobe study. Contributions to Mineralogy and Petrology, 114, 441–451.

Booth, A., Kolodny, Y., Chamberlain, C.P., McWilliams, M., Schmitt, A.K., and Wooden, J. (2005) Oxygen isotopic composition and U-Pb discordance in zircon. Geochimica et Cosmochimica Acta, 69, 4895–4905.

Caruba, R., Baumer, A., Ganteaume, M., and Iacconi, P. (1985) An experimental study of hydroxyl groups and water in synthetic and natural zircons: a model of the metamict state. American Mineralogist, 70, 1224–1231.

Chakoumakos, B.C., Murakami, T., Lumpkin, G.R., and Ewing, R.C. (1987) Alpha-decay-induced fracturing in zircon: the transition from the crystalline to the metamict state. Science, 236, 1556–1559.

Cherniak, D.J. and Watson, E.B. (2001) Pb diffusion in zircon. Chemical Geology, 172, 5–24.

Christenhuss, R. (1968) Zur Darstellbarkeit kristalliner Objekte in der Auflicht-Elektronenmikroskopie. Beiträge zur elektronenmikroskopischen Direktabbildung von Oberflächen, 1, 67–77.

Corfu, F., Hanchar, J.M., Hoskin, P.W.O., and Kinny, P. (2003) Atlas of zircon textures. In J.M. Hanchar and P.W.O. Hoskin, Eds., Zircon, 53, p. 469–500. Reviews in Mineralogy and Geochemistry, Mineralogical Society of America, Chantilly, Virginia.

Crowley, J.L. (2003) U-Pb geochronology of 3810–3630 Ma granitoid rocks south of the Isua greenstone belt, southern West Greenland. Precambrian Research, 126, 235–257.

Davis, D.W. and Edwards, G.R. (1985) The petrogenesis and metallogenesis of the Atikwa-Lawrence volcanic-plutonic terrain. Grant 179, Ontario Geological Survey Miscellaneous Publication 127, 101–111.

Day, A.P. and Quested, T.E. (1999) A comparison of grain imaging and measurement using horizontal orientation and colour orientation contrast imaging, electron backscatter pattern and optical methods. Jornal of Microscopy, 195, 186–196.

Donovan, J.J., Pingitore, N.E., and Westphal, A. (2003) Compositional averaging of back-scatter intensities in compounds. Microscopy and Microanalysis, 9, 202–215.

Ewing, R.C. (1994) The metamict state: 1993—the centennial. Nuclear Instruments and Methods in Physics Research B, 91, 22–29.

Förster, H.-J. (1998) The chemical composition of REE-Y-Th-U-rich accessory minerals in peraluminous granites of the Erzgebirge-Fichtelgebirge region, Germany, Part I: The monazite-(Ce)-brabantite solid solution series. American Mineralogist, 83, 259–272.

Geisler, T., Burakov, B.E., Zirlin, V., Nikolaeva, L., and Pöml, P. (2005) A Raman spectroscopic study of high-uranium zircon from the Chernobyl "lava". European Journal of Mineralogy, 17, 883–894.

Guan, H., Dun, M., Wilde, S.A., Zhou, X., and Zhai, M. (2002) Significance of in situ SIMS chronometry of zoned monazite from the Lewisian granulites, northwest Scotland. Precambrian Research, 113, 1–18.

Hall, M.G. and Lloyd, G.E. (1981) The SEM examination of geological samples with a semiconductor back-scattered electron detector. American Mineralogist, 66, 362–368.

Hanchar, J.M. and Miller, C.F. (1993) Zircon zonation patterns as revealed by cathodoluminescence and back-scattered electron images: Implications for interpretation of complex crustal histories. Chemical Geology, 110, 1–13.

Hanchar, J.M. and Rudnick, R.L. (1995) Revealing hidden structures: The application of cathodoluminescence and back-scattered electron imaging to dating zircons from lower crustal xenoliths. Lithos, 36, 289–303.

Hanchar, J.M., Finch, R.J., Hoskin, P.W.O., Watson, E.B., Cherniak, D.J., and Mariano, A.N. (2001) Rare earth elements in synthetic zircon: Part 1. Synthesis, and rare earth element and phosphorus doping. American Mineralogist, 86, 667–680.

Harangi, S. (2001) Neogene to Quarternary volcanism of the Carpathian-Pannonian region – a review. Acta Geologica Hungarica, 44, 223–258.

Hartmann, L.A., Takehara, L., Leite, J.A.D., McNaughton, N.J., and Vasconcellos, M.A.Z. (1997) Fracture sealing in zircon as evaluated by electron microprobe analyses and back-scattered electron imaging. Chemical Geology, 141, 67–72.

Irber, W., Förster, H.J., Hecht, L., Möller, P., and Morteani, G. (1997) Experimental, geochemical, mineralogical and O-isotope constraints on the late-magmatic history of the Fichtelgebirge granites (Germany). Geologische Rundschau, 86, Supplement, S110–S124.

Irmer, G. (1985) Zum Einfluß der Apparatefunktion auf die Bestimmung von Streuquerschnitten und Lebensdauern aus optischen Phononenspektren. Experimentelle Technik der Physik, 33, 501–506.

Joy, D.C., Newbury, D.E., and Davidson, D.L. (1982) Electron channeling patterns in the scanning electron microscope. Journal of Applied Physics, 53, R81–R122.

Kaneko, Y., Fukui, K., and Hashimoto, S. (2005) Electron channeling contrast imaging of dislocation structures in fatigued austenitic stainless steels. Materials Science and Engineering A, 400–401, 413–417.

Kempe, U., Gruner, T., Nasdala, L., and Wolf, D. (2000) Relevance of cathodoluminescence for the interpretation of U-Pb zircon ages, with an example of an application to a study of zircons from the Saxonian Granulite Complex, Germany. In M. Pagel, V. Barbin, P. Blanc, and D. Ohnenstetter, Eds., Cathodoluminescence in Geosciences, p. 415–455. Springer, Berlin, Heidelberg, New York.

Lehnert, R. (2000) Beyond imagination—image formation based on Raman spectroscopy. GIT Imaging and Microscopy, 2/2000, 6–9.

Lloyd, G.E. (1987) Atomic number and crystallographic contrast images with the SEM: a review of backscattered electron techniques. Mineralogical

Magazine, 51, 3–19.
Lork, A. and Koschek, G. (1991) Einsatz der KL-Technik bei der Beurteilung isotopengeochemisch bestimmter Alter von Zirkonen. Beiträge zur elektronenmikroskopischen Direktabbildung von Oberflächen, 24, 147–166.
Maurice, F., Zemskoff, A., Dorizzi, P., and Poirier, J.P. (1969) Étude de la polygonisation de fluage au moyen des images électroniques au microanalyseur à sonde électronique. Micron, 4, 184–192.
McLelland, J., Morrison, J., Selleck, B., Cunningham, B., Olson, C., and Schmidt, K. (2001) Hydrothermal alteration of late- to post-tectonic Lyon Mountain granitic gneiss, Adirondack Highlands, New York: Origin of quartz-sillimanite segregations, quartz-albite lithologies, and associated Kiruna-type low-Ti Fe-oxide deposits. Journal of Metamorphic Geology, 19, 1–19.
Mitchell, D.R.G. and Day, R.A. (1998) Electron channelling contrast imaging of defect structures in neutron irradiated aluminium. Scripta Materialia, 39, 923–930.
Morrison, D.A., Davis, D.W., Wooden, J.L., Bogard, D.D., Maczuga, D.E., Phinney, W.C., and Ashwal, L.D. (1985) Age of the Mulcahy Lake intrusion, northwest Ontario, and implications for the evolution of greenstone-granite terraines. Earth and Planetary Science Letters, 73, 306–316.
Mosenfelder, J.L. (2000) Pressure dependence of hydroxyl solubility in coesite. Physics and Chemistry of Minerals, 27, 610–617.
Murakami, T., Chakoumakos, B.C., Ewing, R.C., Lumpkin, G.R., and Weber, W.J. (1991) Alpha-decay damage in zircon. American Mineralogist, 76, 1510–1532.
Nasdala, L., Irmer, G., and Wolf, D. (1995) The degree of metamictization in zircon: a Raman spectroscopic study. European Journal of Mineralogy, 7, 471–478.
Nasdala, L., Beran, A., Libowitzky, E., and Wolf, D. (2001a) The incorporation of hydroxyl groups and molecular water in natural zircon ($ZrSiO_4$). American Journal of Science, 301, 831–857.
Nasdala, L., Wenzel, M., Vavra, G., Irmer, G., Wenzel, T., and Kober, B. (2001b) Metamictisation of natural zircon: accumulation vs. thermal annealing of radioactivity-induced damage. Contributions to Mineralogy and Petrology, 141, 125–144.
Nasdala, L., Lengauer, C.L., Hanchar, J.M., Kronz, A., Wirth, R., Blanc, P., Kennedy, A.K., and Seydoux-Guillaume, A.-M. (2002) Annealing radiation damage and the recovery of cathodoluminescence. Chemical Geology, 191, 121–140.
Nasdala, L., Zhang, M., Kempe, U., Panczer, G., Gaft, M., Andrut, M., and Plötze, M. (2003) Spectroscopic methods applied to zircon. In J.M. Hanchar and P.W.O. Hoskin, Eds., Zircon, 53, p. 427–467. Reviews in Mineralogy and Geochemistry, Mineralogical Society of America, Chantilly, Virginia.
Nasdala, L., Hanchar, J.M., Kronz, A., and Whitehouse, M.J. (2005) Long-term stability of alpha particle damage in natural zircon. Chemical Geology, 220, 83–103.
Paterson, B.A., Stephens, W.E., Rogers, G., Williams, I.S., Hinton, R.W., and Herd, D.A. (1992) The nature of zircon inheritance in two granite plutons. Transactions of the Royal Society of Edinburgh, Earth Sciences, 83, 459–471.
Peterman, Z.E., Zartman, R.E., and Sims, P.K. (1986) A protracted Archean history in the Watersmeet gneiss dome, northern Michigan. U.S. Geological Survey Bulletin, 1622, 51–64.
Peucat, J.-J., Capdevila, R., Drareni, A., Choukroune, P., Fanning, C.M., Bernard-Griffiths, J., and Fourcade, S. (1996) Major and trace element geochemistry and isotope (Sr, Nd, Pb, O) systematics of an Archaean basement involved in a 2.0 Ga very high-temperature (1000 °C) metamorphic event: In Ouzzal Massif, Hoggar, Algeria. Journal of Metamorphic Geology, 14, 667–692.
Pointer, C.M., Ashworth, J.R., and Ixer, R.A. (1988) The zircon-thorite mineral group in metasomatized granite, Ririwai, Nigeria. 2. Zoning, alteration and exsolution in zircon. Mineralogy and Petrology, 39, 21–37.
Pouchou, J.-L. and Pichoir, F. (1991) Quantitative analysis of homogeneous or stratified microvolumes applying the method "PAP". In K.F.J. Heinrich and D.E. Newbury, Eds., Electron probe quantitation, p. 31–75. Plenum Press, New York, London.
Prior, D.J., Boyle, A.P., Brenker, F., Cheadle, M.C., Day, A., Lopez, G., Peruzzo, L., Potts, G.J., Reddy, S., Spiess, R., Timms, N.E., Trimby, P., Wheeler, J., and Zetterström, L. (1999) The application of electron backscatter diffraction and orientation contrast imaging in the SEM to textural problems in rocks. American Mineralogist, 84, 1741–1759.
Reddy, S.M., Timms, N.E., Trimby, P., Kinny, P.D., Buchan, C., and Blake, K. (2006) Crystal-plastic deformation of zircon: A defect in the assumption of chemical robustness. Geology, 34, 257–260.
Reiners, P.W., Spell, T.L., Nicolescu, S., and Zanetti, K.A. (2004) Zircon (U-Th)/He thermochronometry: He diffusion and comparisons with $^{40}Ar/^{39}Ar$ dating. Geochimica et Cosmochimica Acta, 68, 1857–1887.
Salje, E.K.H., Chrosch, J., and Ewing, R.C. (1999) Is "metamictization" of zircon a phase transition? American Mineralogist, 84, 1107–1116.
Schwab, A., Bretschneider, J., Buque, C., Blochwitz, C., and Holste, C. (1996) Application of electron channelling contrast to the investigation of strain localization effects in cyclically deformed fcc crystals. Philosophical Magazine Letters, 74, 449–454.
Sergeev, S.A., Komarov, A.N., Bickel, R.A., and Steiger, R.H. (1997) A new microtome for cutting hard submillimeter-sized crystalline objects for promoting high-resolution microanalysis. European Journal of Mineralogy, 9, 449–456.
Simkin, B.A. and Crimp, M.A. (2000) Use of electron channelling contrast imaging to assess near-surface mechanical damage. Philosophical Magazine Letters, 80, 395–400.
Smith, D.G.W., de St. Jorre, L., Reed, S.J.B., and Long, J.V.P. (1991) Zonally metamictized and other zircons from Thor Lake, Northwest Territories. Canadian Mineralogist, 29, 301–309.
Sommerauer, J. (1976) Die chemisch-physikalische Stabilität natürlicher Zirkone und ihr U-(Th)-Pb System. Ph.D. thesis, 151p. Eidgenössische Technische Hochschule, Zürich.
Tichomirowa, M., Berger, H.-J., Koch, E.A., Belyatski, B.V., Götze, J., Kempe, U., Nasdala, L., and Schaltegger, U. (2001) Zircon ages of high-grade gneisses in the Eastern Erzgebirge (Central European Variscides)—constraints on origin of the rocks and Precambrian to Ordovician magmatic events in the Variscan foldbelt. Lithos, 56, 303–332.
Trimby, P. and Prior, D.J. (1999) Microstructural imaging techniques: a comparison between light and scanning electron microscopy. Tectonophysics, 303, 71–81.
Utsunomiya, S., Palenik, C.S., Valley, J.W., Cavosie, A.J., Wilde, S.A., and Ewing, R.C. (2004) Nanoscale occurrence of Pb in an Archean zircon. Geochimica et Cosmochimica Acta, 68, 4679–4686.
Vavra, G., Gebauer, D., Schmid, R., and Compston, W. (1996) Multiple zircon growth and recrystallization during polyphase Late Carboniferous to triassic metamorphism in granulites of the Ivrea Zone (Southern Alps): an ion microprobe (SHRIMP) study. Contributions to Mineralogy and Petrology, 122, 337–358.
Wang, X. and Griffin, W.L. (2004) Unusual Hf contents in metamorphic zircon from coesite-bearing eclogites of the Dabie mountains, east-central China: implications for the dating of ultrahigh-pressure metamorphism. Journal of Metamorphic Geology, 22, 629–637.
Weber, W.J., Ewing, R.C., and Wang, L.-M. (1994) The radiation-induced crystalline-to-amorphous transition in zircon. Journal of Materials Research, 9, 688–698.
Wu, S.D., Wang, Z.G., Jiang, C.B., and Li, G.Y. (2002) Scanning electron microscopy—electron channeling contrast investigation of recrystallization during cyclic deformation of ultrafine grained copper processed by equal channel angular pressing. Philosophical Magazine Letters, 82, 559–565.
Zauter, R., Petry, F., Bayerlein, M., Sommer, C., Christ, H.-J., and Mughrabi, H. (1992) Electron channelling contrast as a supplementary method for microstructural investigations in deformed metals. Philosophical Magazine A, 66, 425–436.
Zhu, X.K., O'Nions, R.K.O., Belshaw, N.S., and Gibb, A.J. (1997) Significance of in situ SIMS chronometry of zoned monazite from the Lewisian granulites, northwest Scotland. Chemical Geology, 135, 35–53.

MANUSCRIPT RECEIVED FEBRUARY 16, 2006
MANUSCRIPT ACCEPTED JUNE 14, 2006
MANUSCRIPT HANDLED BY BRYAN CHAKOUMAKOS